ACS APPLIED MATERIALS & INTERFACES

www.acsami.org

Research Article

Study of Chitosan-Stabilized $Ti_3C_2T_x$ MXene for Ultrasensitive and Interference-Free Detection of Gaseous H_2O_2

Jelena Isailović, Ana Oberlintner, Uroš Novak, Matjaž Finšgar, Filipa M. Oliveira, Jan Paštika, Zdeněk Sofer, Nikola Tasić, Rui Gusmão,* and Samo B. Hočevar*

Cite This: *ACS Appl. Mater. Interfaces* 2023, 15, 31643−31651

Read Online

ACCESS | Metrics & More | Article Recommendations | Supporting Information

ABSTRACT: The development of sensitive, selective, and reliable gaseous hydrogen peroxide (H_2O_2) sensors operating at room temperature still represents a remaining challenge. In this work, we have investigated and combined the advantageous properties of a two-dimensional $Ti_3C_2T_x$ MXene material that exhibits a large specific surface area and high surface activity, with favorable conducting and stabilizing properties of chitosan. The MXene−chitosan membrane was deposited on the ferrocyanide-modified screen-printed working carbon electrode, followed by applying poly(acrylic acid) as an electrolyte and accumulation medium for gaseous H_2O_2. The sensor showed highly sensitive and selective electroanalytical performance for detecting trace concentrations of gaseous H_2O_2 with a very low detection limit of 4 μg m^{-3} (4 ppbv), linear response in the studied concentration range of 0.5−30.0 mg m^{-3}, and good reproducibility with an RSD of 1.3%. The applicability of the sensor was demonstrated by point-of-interest detection of gaseous H_2O_2 during the real hair bleaching process with a 9 and 12% H_2O_2 solution.

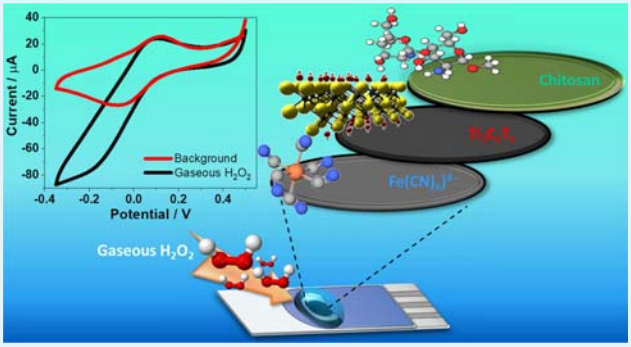

KEYWORDS: *$Ti_3C_2T_x$ MXene, chitosan, hydrogen peroxide, gas sensor, cyclic voltammetry*

INTRODUCTION

In recent years, MXenes have attracted immense attention due to their high metallic conductivity, hydrophilicity, low diffusion barrier, high ion transport properties, biocompatibility, large surface area, and ease of functionalization and thus can serve as a remarkable interface for the development of next-generation sensing strategies.[1−4] This novel class of two-dimensional (2D)-layered materials consists of transition metal carbides or nitrides, with the general formula $M_{n+1}X_nT_x$, where M stands for the transition metal (e.g., Ti, Zr, V, Cr, Nb), X is carbon or nitrogen, and T corresponds to different terminal groups, e.g., O, F, OH, and Cl.[3] Etching of A elements in the MAX phase (A is a p-block element) yields the designated MXenes, as introduced by Gogotsi et al.[5] To date, more than twenty different MXene compounds have been successfully synthesized from the precursor MAX phases by etching and exfoliation methods,[3,6,7] resulting in surface-functionalized MXenes with abundant terminal groups that account for their hydrophilic nature. As such, MXenes can selectively absorb biomolecules and gas molecules through morphology control and surface modification.[8−10] The drawback is that MXenes are highly susceptible to oxidative degradation, leading to impaired functionality and inefficacy. Research efforts related to the specifics of synthesis protocols, storage conditions, or storage media appear to offer some comfort regarding their stability during preparative steps.[11,12] However, for electroanalytical applications, when MXenes are incorporated on the supporting electrodes and subjected to measurements in wide potential windows, an additional application obstacle arises from their innate and irreversible electrooxidation.[13] The existing literature does not yet offer a convincing solution to this problem, which was also addressed in this study.

H_2O_2 is an important molecule that plays a vital role in various fields, such as medicine, clinical diagnostics, biotechnology, chemical synthesis, textile, wood, food, and pharmaceutical industries in the production of cosmetics, dyes, detergents, etc.[14−17] Besides its main property as an oxidant, H_2O_2 is a key molecule in numerous biological systems involving the enzymatic activity of, e.g., oxidases and peroxidases.[18] It is essential as a signaling molecule in the biological processes of the immune system, apoptosis, and root growth.[19,20] As a biomarker, H_2O_2 is associated with oxidative

Received: April 13, 2023
Accepted: June 13, 2023
Published: June 23, 2023

stress[21,22] and, as a gaseous molecule, with several diseases such as lung cancer and other pulmonary disorders.[23−27] In atmospheric processes, gaseous H_2O_2 accompanies reactions involving UV radiation, free radicals, and the transformation of gaseous pollutants. Its occurrence may also indicate the presence of relatively labile peroxo-explosives.[28] Conventional analytical methods typically used for the determination of H_2O_2 include spectroscopy,[29−31] chemiluminescence,[24,32−34] colorimetry,[35] fluorimetry,[36] gas chromatography−mass spectrometry (GC−MS),[37] and others.[38,39] Most of these techniques can achieve satisfactory detection limits, sensitivity, and selectivity; however, expensive and robust equipment, limited portability, and relatively complex sample preparation are persistent challenges that must be overcome. On the other hand, electrochemical sensing offers an attractive alternative to conventional methods, especially in terms of low-cost and compact instrumentation, portability, capability for point-of-interest detection, sensitivity, and relative ease of operation.[40] Many powerful electrochemical sensors have been developed for the detection of H_2O_2 in liquid samples, incorporating numerous redox modifiers, metal, metal oxide, and nonmetallic nanoparticles, enzymes, polymeric membranes, and combinations thereof.[41,42] However, to the best of our knowledge, there are very few reports of electrochemical sensors for detecting considerably more challenging gaseous H_2O_2.[43−48]

In this work, we have investigated the integration of $Ti_3C_2T_x$ MXene into the sensing membrane to construct a disposable, ultrasensitive, and interference-free electrochemical sensor for onsite detection of gaseous H_2O_2. Moreover, through a synergistic effect between $Ti_3C_2T_x$ MXene and chitosan membrane, we successfully stabilized the 2D-layered MXene. We exploited the electrocatalytic characteristics of MXene by combining it with a ferrocyanide-modified working carbon electrode and poly(acrylic acid), the latter simultaneously serving as a suitable accumulation and electrolyte medium for gaseous H_2O_2. We characterized the sensing interface, including the interaction between chitosan and MXene and the stabilization of MXene.

EXPERIMENTAL SECTION

Apparatus. Electrochemical studies were carried out using a portable potentiostat/galvanostat PalmSens4 (PalmSens BV, Houten, Netherlands) in combination with a cable connector for screen-printed electrodes (DRP-CAC 71606, Metrohm DropSens, Herisau, Switzerland) and PSTrace 5.9 software (PalmSens BV). The supporting screen-printed electrode system consisted of a ferrocyanide-bulk-modified carbon working electrode (FCN-SPCE, the diameter of the working electrode was 4 mm), a silver quasi-reference electrode, and a carbon counter electrode (DRP-F10, Metrohm DropSens) designed to work with microvolume solution droplets.

Reagents and Solutions. Methanol (VWR International, Radnor, Pennsylvania), ethanol, benzene (Carlo Erba Reagents, Milano, Italy), H_2O_2 (30%), ammonia, formaldehyde, nitric acid (65%), glycerol, sulfuric acid (95−98%) (all from Merck, Rahway, New Jersey), phenol, high-molecular-weight chitosan (310−375 kDa; ≥75% deacetylated), lactic acid (85%), and sodium nitrite (97%) (all from Sigma-Aldrich, St. Louis, Missouri) were of the analytical grade purity. Pure O_2 (N5.0) was purchased from Messer (Frankfurt, Germany). The chitosan blend (CHI) was prepared as follows: 1.5% (w/v) chitosan and 30.0% (w/w) glycerol were dissolved in 100.0 mL of 1.0% (v/v) aqueous solution of lactic acid, and the mixture was continuously stirred (Ika, Staufen, Germany) overnight at room temperature (24 °C), as reported previously.[49] Test solutions yielding the desired gaseous-phase H_2O_2 concentrations above the solution were prepared in 100.0 mL glass flasks according to Henry's law[50] in the presence of the ambient atmosphere, i.e., no purging was applied. The corresponding Henry constants were given in ref 50. All solutions used in this work were prepared using water purified with the Elix 10/Milli-Q Gradient unit (Millipore, Bedford).

Synthesis and Characterization of the $Ti_3C_2T_x$ MXene. For MXene synthesis, 5.0 g of Ti_3AlC_2 MAX phase material (Jinzhou Haixin Metal Materials, China) was immersed in 250.0 mL of hydrofluoric acid solution (Sigma-Aldrich) with 40.0 vol % and stirred continuously for four days. Then, the sample was stirred for two days in lithium fluoride/hydrochloric acid. Finally, the sample was subjected to iterative cycles of centrifugation and redispersement in water until obtaining a neutral pH value in the residual water. The obtained sample was dried for 24 h in a vacuum oven set at 50 °C.

The morphology of $Ti_3C_2T_x$ MXene was examined by scanning electron microscopy (SEM) with a field emission gun (FEG) electron source (Tescan Lyra dual-beam microscope) at 5 kV acceleration voltage. Elemental composition was investigated by energy-dispersive X-ray spectroscopy (EDXS) using an X-Max^N detector from Oxford Instruments at 20 kV acceleration voltage. For both SEM and EDXS analyses, the colloidal suspension of $Ti_3C_2T_x$ MXene was drop-cast on carbon tape. STEM was performed with the same instrument as SEM but with a STEM sample holder. Diluted suspension of Mxene was drop-cast on a 200 mesh Cu TEM grid and then dried. STEM measurements were carried out using a 30 kV electron beam.

X-ray diffraction (XRD) measurements were carried out using a Bruker D8 Discoverer (Bruker, Germany) diffractometer in Bragg−Brentano parfocal geometry equipped with a Cu Kα radiation source (λ = 0.15418 nm, U = 40 kV, and I = 40 mA). The diffraction pattern was acquired in the scan range of 2θ from 5 to 70° at room temperature. The data were evaluated by HighScore Plus 4.9 software. For the sample preparation, 3.0 μL of a colloidal suspension of $Ti_3C_2T_x$ MXene was drop-cast on a Si/SiO_2 substrate, followed by evaporation of the solvent at room temperature.

An InVia Raman microscope (Renishaw, England) was used for Raman spectroscopy measurements in backscattering geometry with a CCD detector. An Nd:YAG laser (532 nm, 50 mW) with a 2400 line mm^{-1} diffraction grating, an applied power of 1.25%, and a 20x objective were used for the measurements. The Raman spectrum was collected with 200 accumulations in the Raman range of 100−800 cm^{-1} at room temperature. For the sample preparation, the same procedure was used as in the case of XRD measurements.

Atomic force microscopy (AFM) measurements were carried out on a Ntegra Spectra from NT-MDT in a tapping mode using a cantilever with a strain constant of 1.5 kN m^{-1} equipped with a standard silicon tip with a curvature radius less than 10 nm. Sample suspensions of exfoliated material were prepared and drop-cast on a freshly cleaved mica substrate. The measurements were carried out under ambient conditions with a scan rate of 1 Hz and 512 scan lines.

Modification of the Working Electrode and Fabrication of the Sensor. The working electrode was first modified with $Ti_3C_2T_x$ MXene. Before the modification, the MXene solution was sonicated and stirred for 3 min, followed by drop-casting 1.0 μL of the 250.0 mg mL^{-1} solution on the surface of the FCN-SPCE. After drying in air for 10 min, an 8.0 μL droplet of chitosan blend (CHI, from the Reagents and Solutions section) was applied to the working electrode, i.e., on the top of the MXene layer. After drying under laboratory conditions overnight, the whole screen-printed electrode system was modified via drop-casting 20.0 μL of a viscous mixture consisting of 1.0 g of polyacrylic acid (450.000 g mol^{-1}; Sigma-Aldrich) and 10.0 mL of 0.1 M phosphate buffer solution (pH = 7.2), resulting in a polyacrylic gel-like accumulation/electrolyte membrane.

XPS Measurements. XPS measurements were performed with a Supra plus device (Kratos, Manchester, UK) equipped with an Al Kα excitation source. During the spectra acquisition, the charge neutralizer was on. The binding energy scale was corrected using the C−C/C−H peak at 284.8 eV in the C 1s spectra. The screen-printed electrodes were attached to the sample holder using carbon tape. Measurements were carried out at a 90° take-off angle at a pass energy of 20.0 eV and a step of 0.1 eV. The analysis area was 300 by

https://doi.org/10.1021/acsami.3c05314
ACS Appl. Mater. Interfaces 2023, 15, 31643−31651

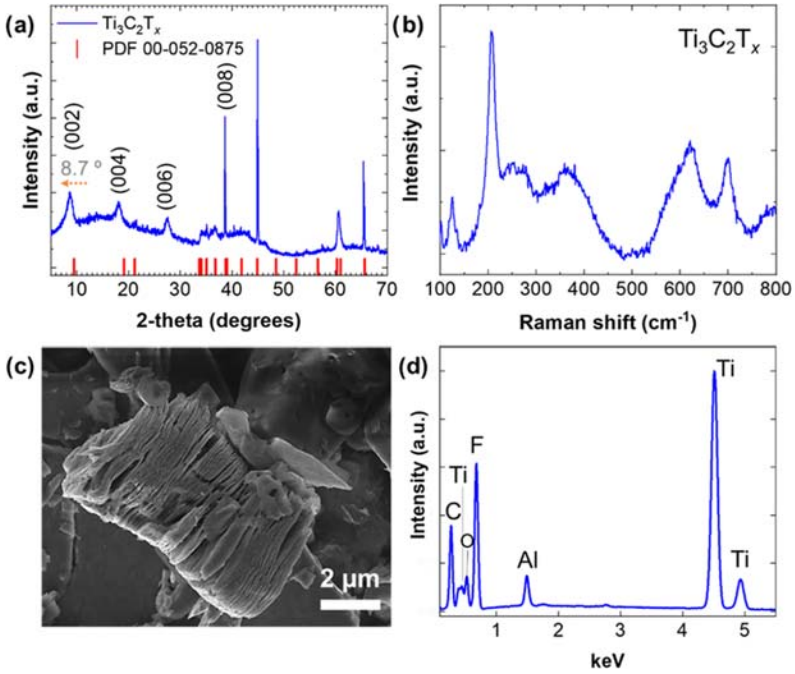

Figure 1. Structural and morphological characterization of $Ti_3C_2T_x$ MXene by XRD (a), Raman spectroscopy (b), SEM (c), and EDXS (d).

700 μm. Spectra were measured and processed using ESCApe 1.5 software (Kratos).

ToF-SIMS Measurements. ToF-SIMS measurements were performed with an M6 device (IONTOF, Münster, Germany). During the spectra acquisition, the flood gun was on. The spectra were calibrated using the peak for CH_3^+ at m/z 15.02, $C_2H_3^+$ at m/z 27.02, and $C_4H_7^+$ at m/z 55.05. The 30.0 keV Bi^+ with a target current of 1.2 pA was employed as the primary ion beam. Sputtering was performed on 500 by 500 μm using the 5.0 keV Ar_{1200}^+ gas cluster ion beam (GCIB), while the analysis was carried out on a 300 by 300 μm in the center of the sputter crater. Spectra were measured and processed, and 3D profiles were constructed using SurfaceLab 7.3 software (IONTOF). The depth (z-scale) of the sputter crater created by the ToF-SIMS sputtering was analyzed using a DektakXT stylus profilometer (Bruker, Karlsruhe, Germany).

Electrochemical Measurements. Cyclic voltammetric measurements were carried out in a potential range of +0.50 to −0.35 V (unless otherwise specified) using a scan rate of 100 mV s^{-1} vs Ag quasi-reference electrode. The gas sensor attached to the electrode holder was inserted tightly into the narrow opening of the chamber, created specifically for the dimensions of a screen-printed electrode, in the area above the solution. All measurements were performed at room temperature (22−23 °C) in a model atmosphere (unless otherwise specified) above the corresponding H_2O_2 solution in the presence of atmospheric gases. For studying the stabilization effect of chitosan on $Ti_3C_2T_x$ MXene, square-wave voltammetry was used in the range of −0.5 to +1.0 V vs Ag quasi-reference electrode.

RESULTS AND DISCUSSION

Characterization of $Ti_3C_2T_x$ MXene. The $Ti_3C_2T_x$ MXene was obtained by selectively etching the Ti_3AlC_2 MAX phase as described in the Experimental Section and illustrated in Scheme S1. The physical and chemical properties of the obtained $Ti_3C_2T_x$ MXene were investigated by X-ray diffraction (XRD), Raman spectroscopy, scanning electron microscopy (SEM) combined with X-ray spectroscopy (EDXS), and atomic force microscopy (AFM).

The XRD pattern of $Ti_3C_2T_x$ MXene is shown in Figure 1a, and its successful synthesis is confirmed by the presence of characteristic diffraction peaks at 8.7, 18.2, 27.6, and 38.6°, which are related to the (002), (004), (006), and (008) planes of this MXene, respectively.[51] For a better understanding of the successful synthesis of $Ti_3C_2T_x$, the powder diffraction file (PDF) of its precursor MAX phase Ti_3AlC_2 (PDF 00-052-0875) was included for comparison. The selective etching of aluminum (Al) is confirmed by a noticeable shift in the (002) diffraction of Ti_3AlC_2 from 9.5 to 8.7° in $Ti_3C_2T_x$. This downshift not only signifies the removal of Al but also indicates the introduction of surface terminations (T_x = −F, −O) in the structural composition of $Ti_3C_2T_x$.

The Raman spectrum in Figure 1b is in agreement with previous studies[52,53] on the vibration modes of $Ti_3C_2T_x$ flakes because typical vibrations related to titanium A_{1g}(Ti, C, O) at 206.5 cm^{-1} and broad peaks in the region of 230−470 cm^{-1} assigned to in-plane (E_g) modes of surface groups attached to Ti atoms are identified. In the 580−730 cm^{-1} region, also designated as the carbon region, the peaks occurring at 621.3 and 700.3 cm^{-1} are associated, respectively, with the vibrations of Ti (E_g) and C (A_{1g}). The peak at 126.1 cm^{-1} is a characteristic resonant peak of laser use during the measurements.[53] The numerical data regarding the identified vibrational modes are summarized in Table S1 and are compared with the reported literature.[52,53] The observed deviations between the Raman spectrum obtained in this work and those reported in the literature (see Table S1) can be attributed to differences arising from material purities and the presence and abundance of terminal groups. Additionally, deviations between experimental results from stacked sheets and theoretical calculations performed on residual-stress-free monosheet models should also be taken into consideration.[52] SEM analysis showed that most Al layers of the Ti_3AlC_2 MAX phase were eliminated after the etching procedure, obtaining the typical accordion-like morphology of the multilayer $Ti_3C_2T_x$ MXene (Figure 1c).[51] The EDXS spectra performed within the same view field (Figure 1d) confirmed the expected C/Ti atomic concentration ratio of 2:3 for $Ti_3C_2T_x$ MXene

https://doi.org/10.1021/acsami.3c05314
ACS Appl. Mater. Interfaces 2023, 15, 31643−31651

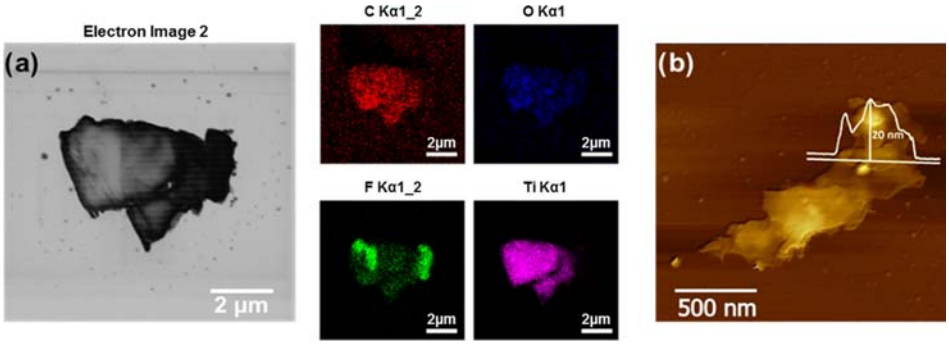

Figure 2. Characterization of $Ti_3C_2T_x$ MXene flakes: STEM image and respective mapping of elements; the scale bar represents 2 μm (a). AFM image with a height profile; the scale bar represents 500 nm (b).

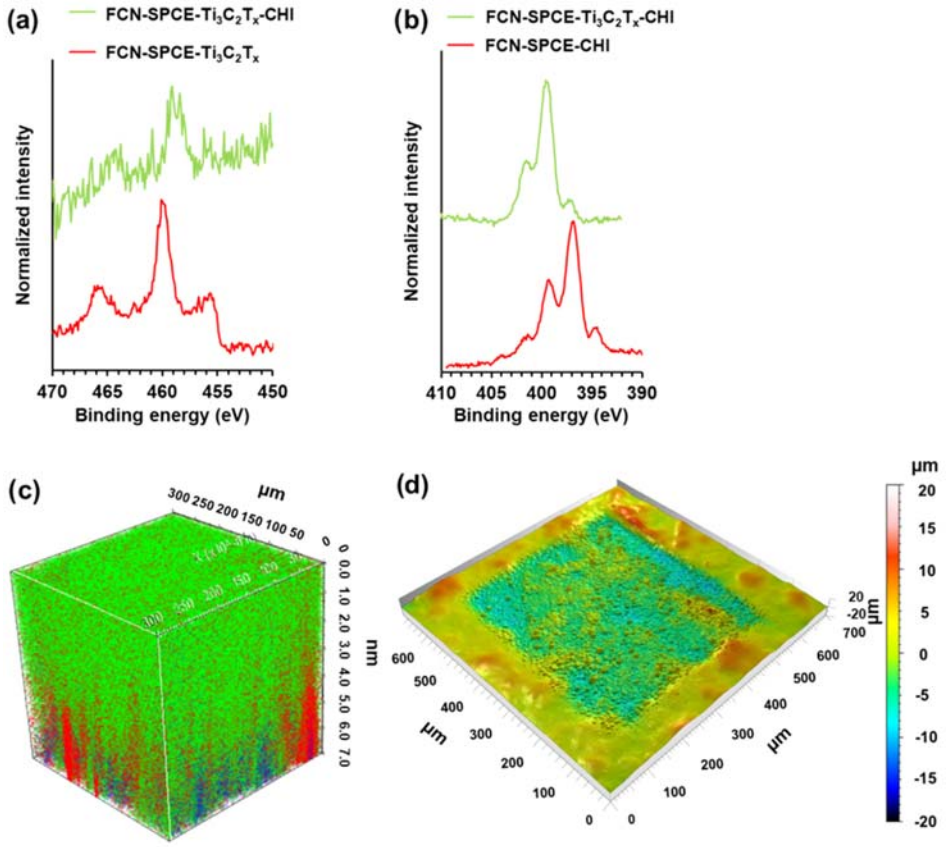

Figure 3. High-resolution Ti 2p (a) and N 1s (b) XPS spectra of FCN-SPCE-$Ti_3C_2T_x$-CHI (green) and FCN-SPCE-$Ti_3C_2T_x$ (red) (a) and FCN-SPCE-$Ti_3C_2T_x$-CHI (green) and FCN-SPCE-CHI (red) (b). 3D ToF-SIMS image of the FCN-SPCE coated with CHI (green), $Ti_3C_2T_x$ MXene (red), and ferrocyanide (blue) (c) and the sputter crater in the sensing membrane measured with a stylus profilometer (d).

besides the residual presence of Al (Table S2). The spectra also show O and F due to their presence as MXene surface terminations (T_x = −OH, −O, −F, etc.). An example of SEM-EDX elemental mapping of $Ti_3C_2T_x$ MXene is shown in Figure S1.

Separated $Ti_3C_2T_x$ MXene flakes were obtained after sonication to form a stable suspension, as observed by STEM and shown in Figures 2a and S2, which typically exhibited micron size in the lateral scale. The elemental maps confirm the composition and distribution of Ti, C, and O, although there was a nonuniform structural feature of F in the $Ti_3C_2T_x$ MXene flake (Figure 2a). The selected elemental line profiles of Ti and C within the same region show a clear higher intensity of both elements within a length of 2.8 μm (Figure S3); positions with a higher Ti concentration match those with a higher C concentration. The AFM image (Figure 2b) shows the corresponding height profile of the $Ti_3C_2T_x$ MXene flake, up to 20 nm, with a lateral size of approximately 1.5 μm. The layer number can be estimated from the theoretical value for a single layer of $Ti_3C_2T_x$ (ca. 0.9 nm) and the measured flake thickness which points to ca. 22 layers. In practical terms, gaps occur between some of the layers, which can be seen in SEM images (Figures 1c and S1); thus, it is possible that the actual number of layers can be lower than the predicted.

Surface Analysis. Figure 3a shows high-resolution Ti 2p spectra for the ferrocyanide-modified screen-printed carbon

https://doi.org/10.1021/acsami.3c05314
ACS Appl. Mater. Interfaces 2023, 15, 31643−31651

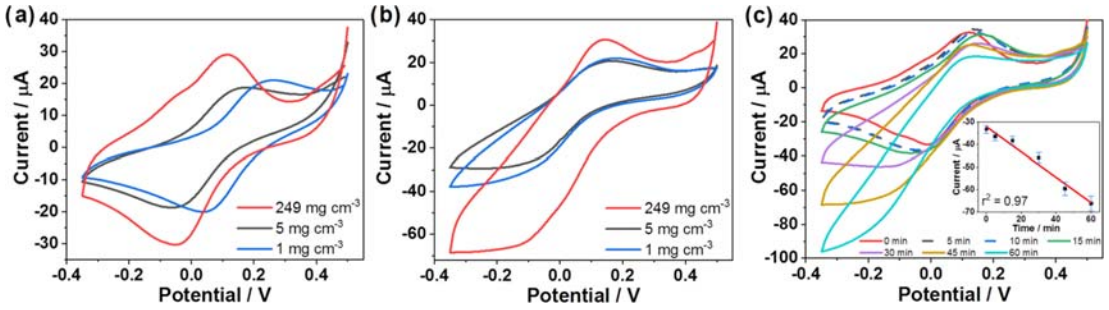

Figure 4. Cyclic voltammograms (CVs) recorded with the sensors prepared using different concentrations of MXene in the absence (a) and presence (b) of 10 mg m^{-3} gaseous H_2O_2 using a 20 min accumulation and a scan rate of 100 mV s^{-1}. CVs recorded for successive increments of accumulation time in the range of 0−60 min together with a background response (red) for 5 mg m^{-3} gaseous H_2O_2 using a scan rate of 100 mV s^{-1} (c) (seven different sensors were used per each time point). All experiments were carried out using completely assembled sensors (FCN-SPCE-MXene-CHI).

electrode (FCN-SPCE) coated with $Ti_3C_2T_x$ (FCN-SPCE-$Ti_3C_2T_x$) and the FCN-SPCE electrode coated with $Ti_3C_2T_x$ and chitosan (CHI), i.e., FCN-SPCE-$Ti_3C_2T_x$-CHI. The main Ti 2p peak for FCN-SPCE-$Ti_3C_2T_x$ is located at 460.0 eV, whereas the Ti 2p spectrum for the electrode that was additionally coated with CHI, i.e., FCN-SPCE-$Ti_3C_2T_x$-CHI, shifts to more negative binding energies, which suggest bonding of Ti-containing species and CHI.

A higher degree of noise is present in the Ti 2p spectrum for FCN-SPCE-$Ti_3C_2T_x$-CHI as $Ti_3C_2T_x$ was underneath the CHI layer, and less signal was obtained for Ti 2p. Figure 3b shows N 1s spectra for the FCN-SPCE electrode coated with CHI (FCN-SPCE-CHI) and the FCN-SPCE electrode coated with $Ti_3C_2T_x$ and CHI (FCN-SPCE-$Ti_3C_2T_x$-CHI). The main peak in the N 1s spectrum for FCN-SPCE-CHI is located at 397.0 eV, while this main peak for FCN-SPCE-$Ti_3C_2T_x$-CHI is shifted to the more positive binding energy. Additional deconvolution of Ti 2p and N 1s spectra with peak assignments is given in the Supporting Information as Figure S5, along with the corresponding discussion. Both peak shifts in the Ti 2p and N 1s spectra indicate that an interaction between CHI and $Ti_3C_2T_x$ occurred, which can explain the electrochemical stabilization of MXene by CHI.

The remarkable stabilization effect was confirmed by the electrochemical characterization of $Ti_3C_2T_x$ MXene in the presence and absence of CHI, as shown in Figure S4. The study compares the square-wave voltammetric responses obtained with bare SPCE (black), CHI-modified SPCE (green), $Ti_3C_2T_x$-modified SPCE (blue), and CHI-$Ti_3C_2T_x$-modified SPCE (red) in 0.1 M KCl as the supporting electrolyte. The signal at ca +0.55 V can be attributed to the typical oxidation of $Ti_3C_2T_x$ MXene deposited on the SPCE.[13] On the other hand, when the $Ti_3C_2T_x$ MXene was codeposited with CHI (red), no oxidation signal was observed at this potential, indicating a favorable stabilization effect of CHI. Clearly, the signal at ca +0.0 V belongs to CHI. In this study, a supporting SPCE was used instead of FCN-SPCE since the latter exhibits a redox activity in the potential window significant for both studied species, i.e., MXene and CHI.

The ToF-SIMS technique was employed to determine the spatial distribution of the species in the gas-sensing membrane. Signals for CH_4N^+ at m/z 30.03, $C_2H_4NO^+$ at m/z 58.03, $C_2H_5NO^+$ at m/z 59.04, $C_3H_6NO^+$ at m/z 72.05, and $C_6H_{10}NO_3^+$ at m/z 144.09[54−57] were used to determine the 3D distribution of chitosan. The spatial distribution of $Ti_3C_2T_x$ was characterized by the signal for Ti^+ at m/z 47.95, and the position of ferrocyanide was characterized by the signal for Fe^+ at m/z 55.94. The obtained depth profile was processed to obtain a 3D image, which is presented in Figure 3c. Chitosan covers the topmost position (green area with a thickness of ca 4 μm), followed by $Ti_3C_2T_x$ (red spots), which is deposited on the ferrocyanide-modified (blue spots) screen-printed carbon electrode. The ToF-SIMS 3D imaging, therefore, confirms the layered design of the sensor, whereas Figure 3d shows the topography of the sensing membrane and the depth of the sputter crater (ca 7 μm) measured by the stylus profilometer.

Electroanalytical Performance. Since the initial experiments showed a positive effect of MXene upon the detection of gaseous H_2O_2, we investigated the cyclic voltammetric behavior of gas sensors that were prepared using different concentrations of MXene in the modification layer.

Figure 4 shows the cyclic voltammetric responses of such gas sensors in the absence (a) and presence (b) of 10 mg m^{-3} gaseous H_2O_2. In the absence of H_2O_2, the sensor revealed two well-developed redox signals corresponding to the oxidation and reduction of $Fe(CN)_6^{4-}/Fe(CN)_6^{3-}$ redox couple between ca +0.00 and −0.20 V vs Ag quasi-reference electrode (Figure 4a). The most pronounced effect of MXene was observed at the highest concentration tested (249 mg cm^{-3}) at the electrode surface, whereas the modification with 5 mg cm^{-3} MXene resulted only in shifted peaks of the $Fe(CN)_6^{4-}/Fe(CN)_6^{3-}$ redox couple toward more negative potentials for ca 100 mV. After only 20 min of exposure to gaseous H_2O_2, a substantial increase in the reduction signal was observed, as shown in Figure 4b.

In the presence of H_2O_2, $(Fe(CN)_6)^{4-}$ is chemically re-oxidized to $(Fe(CN)_6)^{3-}$, followed by immediate electrochemical re-reduction at the electrode surface. Consequently, the voltammogram displayed an increased reduction signal during the cathodic potential scan. It can be perceived that the highest examined concentration of MXene resulted in the highest cathodic response toward gaseous H_2O_2. On the other hand, it is also evident that the sensor containing the highest concentration of MXene exhibited a somewhat higher anodic signal, implying favorable electrocatalytic characteristics of MXene.

To gain further insight into the electroanalytical properties of the gas sensor, we investigated the effect of accumulation time on its voltammetric response; each measurement was performed with a newly fabricated sensor (Figure 4c). It was found that the current signal increased almost linearly with increasing accumulation time in the examined time range of

https://doi.org/10.1021/acsami.3c05314
ACS Appl. Mater. Interfaces 2023, 15, 31643−31651

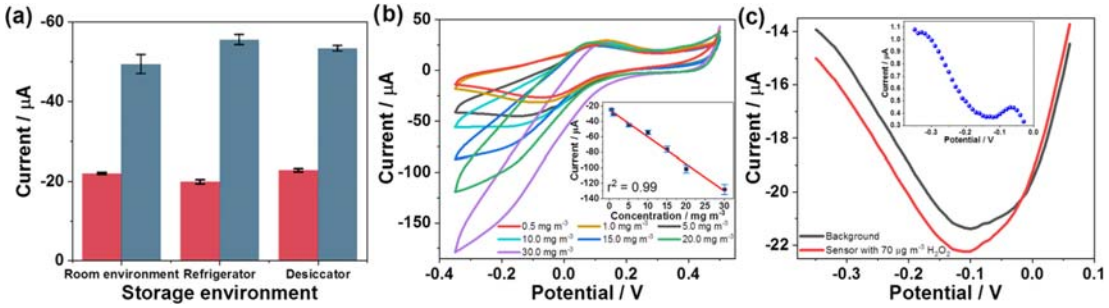

Figure 5. CV signal dependence on different storage conditions in the absence (red) and presence (blue) of 10 mg m^{-3} H_2O_2: refrigerator (ca 4 °C, 65% RH), laboratory (ca 26 °C, 59% RH), and desiccator (ca 26 °C, 10% RH) (a). CVs recorded for successive increments of gaseous H_2O_2 concentrations in the range of 0.5−30.0 mg m^{-3} using a 50 min accumulation and the corresponding calibration plot (b). CVs recorded for 70 μg m^{-3} gaseous H_2O_2 (red) together with background response (black) using a 60 min accumulation; a background subtracted voltammogram is shown in the inset (dotted blue) (c). Other conditions are as in Figure 4c.

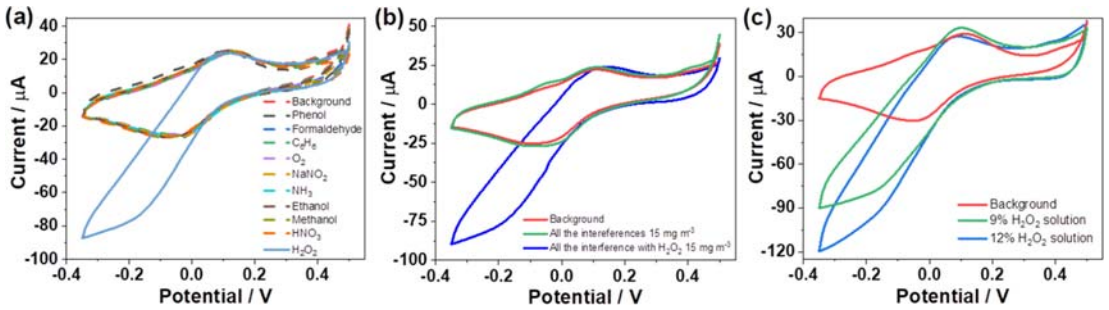

Figure 6. CVs recorded individually for nine potential gaseous interferants of 15 mg m^{-3} each (a) and in the presence of all nine interferants together (of 15 mg m^{-3} each) (b), along with the addition of 15 mg m^{-3} H_2O_2 and a background response using a 20 min accumulation. CVs recorded for a background (red) and when the gas sensor was left for 20 min in a room, where hair bleaching was carried out using 9% (green) and 12% (blue) H_2O_2 solution (c). Other conditions are as in Figure 4c.

0−60 min. In this range, we did not observe any concentration saturation. On the contrary, apart from a linear increase of the signal (r^2 = 0.97) at longer exposure times, excellent reproducibility was observed for each data point, as shown by the small error bars in Figure 4c. An even higher response could be achieved by further increasing the accumulation time; however, considerably longer accumulation times are associated with the inherent instability of gaseous H_2O_2.

With longer accumulation times and consequently with higher concentrations of gaseous H_2O_2 in the sensing membrane, the signal waveform gradually changes from a peak-shaped to a steady state-shaped voltammogram and then, with even longer accumulation times, to a situation with a well-visible deflection point. This process is also accompanied by a gradual shift of the reduction potential toward more negative values. This is due to the change in the diffusion profile with more accumulated H_2O_2 and electrogenerated product as a result of H_2O_2 reduction in the vicinity of the electrode surface, along with the inherently irreversible reduction reaction of H_2O_2.

In addition, the stability study of the sensor was conducted at various temperatures and humidity, as shown in Figure 5a. The sensors were stored overnight in different environments, i.e., in the laboratory, refrigerator, and desiccator; they were tested in triplicate. It can be observed that the background responses of the sensors stored in different ways are practically the same, i.e., within the range of standard deviation. Interestingly, storage in the desiccator did not affect the sensor response, i.e., the dry atmosphere did not compromise the electroanalytical performance of the gas sensor. A slightly lower response toward the gaseous analyte was observed when the sensor was stored under ambient conditions. This could be due to the combination of higher ambient humidity and temperature (at more than 5 °C), which could accelerate the hydrolytic damage degree of the chitosan and change its physicochemical properties.[58,59]

We followed the performance of the sensor in terms of its response to increasing concentrations of gaseous H_2O_2. In combination with a 50 min accumulation, the sensor exhibited a well-developed and satisfactory linear response in the examined concentration range of 0.5−30 mg m^{-3} with r^2 of 0.99 (Figure 5b). The deviation from the higher linearity is due to the accumulation/dissolution/diffusion pattern of H_2O_2 in the viscous sensing membrane and the partial decomposition of relatively unstable H_2O_2.

The gas sensor was also successfully tested for the detection of lower H_2O_2 concentration; as depicted in Figure 5c, a well-readable voltammetric signal was obtained for 70 μg m^{-3} in conjunction with an accumulation time of only 60 min. The sensor unveiled a very low limit of detection (3σ criterion) of 4 μg m^{-3}. Moreover, surprisingly, good sensor-to-sensor repeatability was achieved, with a relative standard deviation (RSD) of only 1.30% when measuring 70 μg m^{-3} gaseous H_2O_2.

Selectivity Study. The operation of the gas sensor was investigated in the presence of selected potential gaseous compounds expected in the real environment. The study was performed by measuring the potential interferants individually at a concentration of 15 mg m^{-3} each, followed by the addition of 15 mg m^{-3} H_2O_2, as shown in Figure 6a.

https://doi.org/10.1021/acsami.3c05314
ACS Appl. Mater. Interfaces 2023, 15, 31643−31651

In the absence of gaseous H_2O_2, no analytical signal was detected for gaseous methanol, ethanol, formaldehyde, phenol, ammonia, benzene, oxygen, nitric acid, and sodium nitrite in the applied potential range of +0.50 to −0.35 V. In addition, the sensor was exposed to a mixture of all of these gaseous compounds at a concentration of 15 mg m^{-3} each. After the addition of 15 mg m^{-3} H_2O_2, a well-defined reduction signal of H_2O_2 was formed with no visible effects of the nine gaseous compounds present, confirming the excellent selectivity of the gas sensor (Figure 6b).

Real Sample Detection. Finally, the performance of the gas sensor was tested in a real environment during the bleaching treatment of human hair. The experiment was carried out in a fume hood by applying 10.0 mL of a 9% H_2O_2 solution to the wig; each of the three sensors was exposed for 20 min. After washing and drying the wig, the same procedure was repeated with 10.0 mL of a 12% H_2O_2 solution (Figure 6c). In both cases, the background was measured in the absence of gaseous H_2O_2. The sensor exhibited distinct signals for both concentrations of gaseous H_2O_2; after three successive measurements, an average determined concentration of ca 18 mg m^{-3} for 9% H_2O_2 solution and ca 24 mg m^{-3} for 12% H_2O_2 solution was obtained.

CONCLUSIONS

In this work, we have demonstrated a synergistic effect of the advantageous physicochemical properties of exfoliated $Ti_3C_2T_x$ MXene and the stabilizing characteristics of chitosan, together with the redox activity of the ferrocyanide-modified screen-printed carbon electrode for ultrasensitive point-of-interest detection of gaseous H_2O_2. The poly(acrylic acid)-based membrane served simultaneously as an electrolyte and a suitable accumulation medium for the gaseous analyte. The sensor showed excellent interference-free operation in the cathodic potential range along with good sensor-to-sensor reproducibility, favorable stability, and a very low detection limit of only 4 μg m^{-3} (ppbv). The applicability of the $Ti_3C_2T_x$ MXene-based gas sensor was successfully demonstrated by measuring H_2O_2 during the treatment of real human hair with a bleaching agent.

ASSOCIATED CONTENT

Supporting Information

The Supporting Information is available free of charge at https://pubs.acs.org/doi/10.1021/acsami.3c05314.

Synthesis route to prepare $Ti_3C_2T_x$ MXene from the precursor Ti_3AlC_2 MAX phase (Scheme S1); SEM micrograph of $Ti_3C_2T_x$ MXene and mapping of elements (Figure S1); bright-mode STEM image of $Ti_3C_2T_x$ MXene flakes (Figure S2); mapping of elements of $Ti_3C_2T_x$ MXene flakes and relative intensity profiles (Figure S3); Raman shift positions for Raman-active modes of $Ti_3C_2T_x$ (Table S1); EDXS element quantification of $Ti_3C_2T_x$ MXene (Table S2); square-wave voltammograms of MXene stabilization study (Figure S4); and deconvolution of the high-resolution Ti 2p XPS spectra and N 1s XPS spectra for sensing layers (Figure S5) (PDF)

AUTHOR INFORMATION

Corresponding Authors

Rui Gusmão − *Department of Inorganic Chemistry, University of Chemistry and Technology Prague, 16628 Prague, Czech Republic;* orcid.org/0000-0001-6358-7601; Email: rui.gusmao@vscht.cz

Samo B. Hočevar − *Department of Analytical Chemistry, National Institute of Chemistry, 1000 Ljubljana, Slovenia;* orcid.org/0000-0003-2980-4822; Email: samo.hocevar@ki.si

Authors

Jelena Isailović − *Department of Analytical Chemistry, National Institute of Chemistry, 1000 Ljubljana, Slovenia; International Postgraduate School Jožef Štefan, 1000 Ljubljana, Slovenia*

Ana Oberlintner − *International Postgraduate School Jožef Štefan, 1000 Ljubljana, Slovenia; Department of Catalysis and Chemical Reaction Engineering, National Institute of Chemistry, 1000 Ljubljana, Slovenia*

Uroš Novak − *Department of Catalysis and Chemical Reaction Engineering, National Institute of Chemistry, 1000 Ljubljana, Slovenia;* orcid.org/0000-0003-0561-8427

Matjaž Finšgar − *Faculty of Chemistry and Chemical Engineering, University of Maribor, 2000 Maribor, Slovenia;* orcid.org/0000-0002-8302-9284

Filipa M. Oliveira − *Department of Inorganic Chemistry, University of Chemistry and Technology Prague, 16628 Prague, Czech Republic;* orcid.org/0000-0001-7268-3144

Jan Paštika − *Department of Inorganic Chemistry, University of Chemistry and Technology Prague, 16628 Prague, Czech Republic*

Zdeněk Sofer − *Department of Inorganic Chemistry, University of Chemistry and Technology Prague, 16628 Prague, Czech Republic;* orcid.org/0000-0002-1391-4448

Nikola Tasić − *Department of Analytical Chemistry, National Institute of Chemistry, 1000 Ljubljana, Slovenia;* orcid.org/0000-0002-0582-2252

Complete contact information is available at: https://pubs.acs.org/10.1021/acsami.3c05314

Notes

The authors declare no competing financial interest.

ACKNOWLEDGMENTS

The work was supported by the Slovenian Research Agency (P1-0034, P2-0118) and the Slovenian Research Agency's Young Researchers Programme (grant agreement no. 52020). The project is co-financed by the Republic of Slovenia, the Ministry of Education, Science and Sport, and the European Union under the European Regional Development Fund. Z.S. was supported by Czech Science Foundation (GAČR No. 20-16124J). J.P. acknowledges support from the grant of specific university research—A2_FCHT_2023_102.

REFERENCES

(1) Ho, D. H.; Choi, Y. Y.; Jo, S. B.; Myoung, J.-M.; Cho, J. H. Sensing with MXenes: Progress and Prospects. *Adv. Mater.* **2021**, *33*, No. 2005846.

(2) Sinha, A.; Dhanjai; Zhao, H.; Huang, Y.; Lu, X.; Chen, J.; Jain, R. MXene: An Emerging Material for Sensing and Biosensing. *TrAC, Trends Anal. Chem.* **2018**, *105*, 424−435.
(3) Verger, L.; Natu, V.; Carey, M.; Barsoum, M. W. MXenes: An Introduction of Their Synthesis, Select Properties, and Applications. *Trends Chem.* **2019**, *1*, 656−669.
(4) Oliveira, F. M.; Gusmão, R. Recent Advances in the Electromagnetic Interference Shielding of 2D Materials Beyond Graphene. *ACS Appl. Electron. Mater.* **2020**, *2*, 3048−3071.
(5) Naguib, M.; Kurtoglu, M.; Presser, V.; Lu, J.; Niu, J.; Heon, M.; Hultman, L.; Gogotsi, Y.; Barsoum, M. W. Two-Dimensional Nanocrystals Produced by Exfoliation of Ti_3AlC_2. *Adv. Mater.* **2011**, *23*, 4248−4253.
(6) Gogotsi, Y.; Anasori, B. The Rise of MXenes. *ACS Nano* **2019**, *13*, 8491−8494.
(7) Haemers, J.; Gusmão, R.; Sofer, Z. Synthesis Protocols of the Most Common Layered Carbide and Nitride MAX Phases. *Small Methods* **2020**, *4*, No. 1900780.
(8) Ding, L.; Wei, Y.; Li, L.; Zhang, T.; Wang, H.; Xue, J.; Ding, L.-X.; Wang, S.; Caro, J.; Gogotsi, Y. MXene Molecular Sieving Membranes for Highly Efficient Gas Separation. *Nat. Commun.* **2018**, *9*, No. 2002.
(9) Lee, E.; Kim, D.-J. Review—Recent Exploration of Two-Dimensional MXenes for Gas Sensing: From a Theoretical to an Experimental View. *J. Electrochem. Soc.* **2020**, *167*, No. 037515.
(10) Dixit, F.; Zimmermann, K.; Alamoudi, M.; Abkar, L.; Barbeau, B.; Mohseni, M.; Kandasubramanian, B.; Smith, K. Application of MXenes for Air Purification, Gas Separation and Storage: A review. *Renewable Sustainable Energy Rev.* **2022**, *164*, No. 112527.
(11) Iqbal, A.; Hong, J.; Ko, T. Y.; Koo, C. M. Improving Oxidation Stability of 2D MXenes: Synthesis, Storage Media, and Conditions. *Nano Convergence* **2021**, *8*, 9.
(12) Habib, T.; Zhao, X.; Shah, S. A.; Chen, Y.; Sun, W.; An, H.; Lutkenhaus, J. L.; Radovic, M.; Green, M. J. Oxidation Stability of $Ti_3C_2T_x$ MXene Nanosheets in Solvents and Composite Films. *npj 2D Mater. Appl.* **2019**, *3*, 8.
(13) Nayak, P.; Yang, M.; Wang, Z.; Li, X.; Miao, R.; Compton, R. G. Single-Entity $Ti_3C_2T_x$ MXene Electro-Oxidation. *Appl. Mater. Today* **2022**, *26*, No. 101335.
(14) Eul, W.; Moeller, A.; Steiner, N.Hydrogen Peroxide *Wiley, Kirk-Othmer Encyclopedia of Chemical Technology* 2000; Vol. *13*, p 1.
(15) Chen, W.; Fan, H.; Balakrishnan, K.; Wang, Y.; Sun, H.; Fan, Y.; Gandhi, V.; Arnold, L. A.; Peng, X. Discovery and Optimization of Novel Hydrogen Peroxide Activated Aromatic Nitrogen Mustard Derivatives as Highly Potent Anticancer Agents. *J. Med. Chem.* **2018**, *61*, 9132−9145.
(16) Müller, G.; Chylenski, P.; Bissaro, B.; Eijsink, V.G.-H.; Horn, S. J. The Impact of Hydrogen Peroxide Supply on LPMO Activity and Overall Saccharification Efficiency of a Commercial Cellulase Cocktail. *Biotechnol. Biofuels* **2018**, *11*, 209.
(17) Holkar, C. R.; Jadhav, A. J.; Pinjari, D. V.; Mahamuni, N. M.; Pandit, A. B. A Critical Review on Textile Wastewater Treatments: Possible Approaches. *J. Environ. Manage.* **2016**, *182*, 351−366.
(18) Giorgio, M.; Trinei, M.; Migliaccio, E.; Pelicci, P. G. Hydrogen Peroxide: A Metabolic By-Product or a Common Mediator of Ageing Signals? *Nat. Rev. Mol. Cell Bio.* **2007**, *8*, 722−728.
(19) Wu, J.; Shu, S.; Li, C.; Sun, J.; Guo, S. Spermidine-Mediated Hydrogen Peroxide Signaling Enhances the Antioxidant Capacity of Salt-Stressed Cucumber Roots. *Plant Physiol. Biochem.* **2018**, *128*, 152−162.
(20) Whittemore, E. R.; Loo, D. T.; Cotman, C. W. Exposure to Hydrogen Peroxide Induces Cell Death via Apoptosis in Cultured Rat Cortical Neurons. *Neuroreport* **1994**, *5*, 1485−1488.
(21) Veal, E. A.; Day, A. M.; Morgan, B. A. Hydrogen Peroxide Sensing and Signaling. *Mol. Cell* **2007**, *26*, 1−14.
(22) Sies, H. Hydrogen Peroxide as a Central Redox Signaling Molecule in Physiological Oxidative Stress: Oxidative Eustress. *Redox Biol.* **2017**, *11*, 613−619.
(23) Zhou, M.; Liu, Y.; Duan, Y. Breath Biomarkers in Diagnosis of Pulmonary Diseases. *Clin. Chim. Acta* **2012**, *413*, 1770−1780.
(24) Zappacosta, B.; Persichilli, S.; Mormile, F.; Minucci, A.; Russo, A.; Giardina, B.; Sole, P. D. A Fast Chemiluminescent Method for H_2O_2 Measurement in Exhaled Breath Condensate. *Clin. Chim. Acta* **2001**, *310*, 187−191.
(25) Stolarek, R.; Bialasiewicz, P.; Krol, M.; Nowak, D. Breath Analysis of Hydrogen Peroxide as a Diagnostic Tool. *Clin. Chim. Acta* **2010**, *411*, 1849−1861.
(26) Svensson, S.; Olin, A. C.; Lärstad, M.; Ljungkvist, G.; Torén, K. Determination of Hydrogen Peroxide in Exhaled Breath Condensate by Flow Injection Analysis with Fluorescence Detection. *J. Chromatogr. B* **2004**, *809*, 199−203.
(27) Chan, H. P.; Lewis, C.; Thomas, P. S. Exhaled Breath Analysis: Novel Approach for Early Detection of Lung Cancer. *Lung Cancer* **2009**, *63*, 164−168.
(28) Klapötke, T. M.; Wloka, T. Peroxide Explosives. *PATAI's Chem. Funct. Groups* **2009**, 1−28.
(29) Meyer, J.; Karst, U. Workplace Monitoring of Gas Phase Hydrogen Peroxide by Means of Fluorescence Spectroscopy. *Anal. Chim. Acta* **1999**, *401*, 191−196.
(30) Voraberger, H.; Ribitsch, V.; Janotta, M.; Mizaikoff, B. Application of Mid-Infrared Spectroscopy: Measuring Hydrogen Peroxide Concentrations in Bleaching Baths. *Appl. Spectrosc.* **2003**, *57*, 574−579.
(31) Stewart, S. P.; Bell, S.E.J.; McAuley, D.; Baird, I.; Speers, S. J.; Kee, G. Determination of Hydrogen Peroxide Concentration Using a Handheld Raman spectrometer: Detection of an Axplosives Precursor. *Forensic Sci. Int.* **2012**, *216*, e5−e8.
(32) Navas, M. J.; Jiménez, A. M.; Galán, G. Air Analysis: Determination of Hydrogen Peroxide by Chemiluminescence. *Atmos. Environ.* **1999**, *33*, 2279−2283.
(33) Li, J.; Dasgupta, P. K. Measurement of Gaseous Hydrogen Peroxide with a Liquid Core Waveguide Chemiluminescence Detector. *Anal. Chim. Acta* **2001**, *442*, 63−70.
(34) Tahirović, A.; Čopra, A.; Omanović-Mikličanin, E.; Kalcher, K. A Chemiluminescence Sensor for the Determination of Hydrogen Peroxide. *Talanta* **2007**, *72*, 1378−1385.
(35) Xu, M.; Bunes, B. R.; Zang, L. Paper-Based Vapor Detection of Hydrogen Peroxide: Colorimetric Sensing with Tunable Interface. *ACS Appl. Mater. Interfaces* **2011**, *3*, 642−647.
(36) Sanchez, J. C.; Trogler, W. C. Polymerization of a Boronate-Functionalized Fluorophore by Double Transesterification: Applications to Fluorescence Detection of Hydrogen Peroxide Vapor. *J. Mater. Chem.* **2008**, *18*, 5134−5141.
(37) Chen, L. C.; Hiroaki, S.; Kunihiko, M.; Osamu, A.; Kenzo, H. Mass Spectrometric Detection of Gaseous Hydrogen Peroxide in Ambient Air Using Dielectric Barrier Discharge as an Excitation Source. *Chem. Lett.* **2009**, *38*, 520−521.
(38) Kirchner, P.; Oberländer, J.; Suso, H-P.; Rysstad, G.; Keusgen, M.; Schöning, M. J. Monitoring the Microbicidal Effectiveness of Gaseous Hydrogen Peroxide in Sterilisation Processes by Means of a Calorimetric Gas Sensor. *Food Control* **2013**, *31*, 530−538.
(39) Steinberg, S. M. High-Performance Liquid Chromatography Method for Determination of Hydrogen Peroxide in Aqueous Solution and Application to Simulated Martian Soil and Related Materials. *Environ. Monit. Assess.* **2013**, *185*, 3749−3757.
(40) Kimmel, D. W.; LeBlanc, G.; Meschievitz, M. E.; Cliffel, D. E. Electrochemical Sensors and Biosensors. *Anal. Chem.* **2012**, *84*, 685−707.
(41) Gulaboski, R.; Mirčeski, V.; Kappl, R.; Hoth, M.; Bozem, M. Review—Quantification of Hydrogen Peroxide by Electrochemical Methods and Electron Spin Resonance Spectroscopy. *J. Electrochem. Soc.* **2019**, *166*, G82.
(42) Yu, Y.; Pan, M.; Peng, J.; Hu, D.; Hao, Y.; Qian, Z. A Review on Recent Advances in Hydrogen Peroxide Electrochemical Sensors for Applications in Cell Detection. *Chin. Chem. Lett.* **2022**, *33*, 4133−4145.

https://doi.org/10.1021/acsami.3c05314
ACS Appl. Mater. Interfaces 2023, 15, 31643−31651

(43) Kuwata, S.; Yoshihiko, S. Detection of Gaseous Hydrogen Peroxide Using Planar-Type Amperometric Cell at Room Temperature. *Sens. Actuators, B* **2000**, *65*, 325−326.
(44) Toniolo, R.; Geatti, P.; Bontempelli, G.; Schiavon, G. Amperometric Monitoring of Hydrogen Peroxide in Workplace Atmospheres by Electrodes Supported on Ion-Exchange Membranes. *J. Electroanal. Chem.* **2001**, *514*, 123−128.
(45) Aroutiounian, V.; Arakelyan, V.; Aleksanyan, M.; Sayunts, A.; Shahnazaryan, G.; Kacer, P.; Picha, P.; Kovarik, J.; Pekarek, J.; Joost, B. Nanostructured Sensors for Detection of Hydrogen Peroxide Vapours. *Sens. Transducers* **2017**, *213*, 46.
(46) Isailović, J.; Vidović, K.; Hočevar, S. B. Simple Electrochemical Sensors for Highly Sensitive Detection of Gaseous Hydrogen Peroxide Using Polyacrylic-Acid-Based Sensing Membrane. *Sens. Actuators, B* **2022**, *352*, No. 131053.
(47) Maier, D.; Laubender, E.; Basavanna, A.; Schumann, S.; Güder, F.; Urban, G. A.; Dincer, C. Toward Continuous Monitoring of Breath Biochemistry: A Paper-Based Wearable Sensor for Real-Time Hydrogen Peroxide Measurement in Simulated Breath. *ACS Sens.* **2019**, *4*, 2945−2951.
(48) Giaretta, J. E.; Oveissi, F.; Dehghani, F.; Naficy, S. Paper-Based, Chemiresistive Sensor for Hydrogen Peroxide Detection. *Adv. Mater. Technol.* **2021**, *6*, No. 2001148.
(49) Bajić, M.; Ročnik, T.; Oberlintner, A.; Scognamiglio, F.; Novak, U.; Likozar, B. Natural Plant Extracts as Active Components in Chitosan-Based Films: A Comparative Study. *Food Packag. Shelf Life* **2019**, *21*, No. 100365.
(50) Sander, R. Compilation of Henry's Law Constants (Version 4.0) for Water as Solvent. *Atmos. Chem. Phys.* **2015**, *15*, 4399−4981.
(51) Alhabeb, M.; Maleski, K.; Anasori, B.; Lelyukh, P.; Clark, L.; Sin, S.; Gogotsi, Y. Guidelines for Synthesis and Processing of Two-Dimensional Titanium Carbide ($Ti_3C_2T_x$ MXene). *Chem. Mater.* **2017**, *29*, 7633−7644.
(52) Hu, T.; Wang, J.; Zhang, H.; Li, Z.; Hu, M.; Wang, X. Vibrational Properties of Ti_3C_2 and $Ti_3C_2T_2$ (T = O, F, OH) Monosheets by First-Principles Calculations: A Comparative Study. *Phys. Chem. Chem. Phys.* **2015**, *17*, 9997−10003.
(53) Sarycheva, A.; Gogotsi, Y. Raman Spectroscopy Analysis of the Structure and Surface Chemistry of $Ti_3C_2T_x$ MXene. *Chem. Mater.* **2020**, *32*, 3480−3488.
(54) Hashmi, A.; Sodhi, R. N. S.; Kishen, A. Interfacial Characterization of Dentin Conditioned with Chitosan Hydroxyapatite Precursor Nanocomplexes Using Time-of-flight Secondary Ion Mass Spectrometry. *J. Endod.* **2019**, *45*, 1513−1521.
(55) D'Almeida, M.; Attik, N.; Amalric, J.; Brunon, C.; Renaud, F.; Abouelleil, H.; Toury, B.; Grosgogeat, B. Chitosan Coating as an Antibacterial Surface for Biomedical Applications. *PLoS One* **2017**, *12*, No. e0189537.
(56) Wu, T.; Du, Y.; Yan, N.; Farnood, R. Cellulose Fiber Networks Reinforced with Glutaraldehyde−Chitosan Complexes. *J. Appl. Polym. Sci.* **2015**, *132*, 42375.
(57) Finšgar, M.; Ristić, T.; Fardim, P.; Zemljič, L. F. Time-of-Flight Secondary Ion Mass Spectrometry Analysis of Chitosan-Treated Viscose Fibres. *Anal. Biochem.* **2018**, *557*, 131−141.
(58) Qin, C. Q.; Du, Y. M.; Xiao, L. Effect of Hydrogen Peroxide Treatment on the Molecular Weight and Structure of Chitosan. *Polym. Degrad. Stab.* **2002**, *76*, 211−218.
(59) Szymańska, E.; Winnicka, K. Stability of Chitosan—A Challenge for Pharmaceutical and Biomedical Applications. *Mar. Drugs* **2015**, *13*, 1819−1846.

https://doi.org/10.1021/acsami.3c05314
ACS Appl. Mater. Interfaces 2023, 15, 31643−31651